

## Imaging $F$ region drifts using monostatic phased-array incoherent scatter radar

T. W. Butler,<sup>1</sup> J. Semeter,<sup>1</sup> C. J. Heinselman,<sup>2</sup> and M. J. Nicolls<sup>2</sup>

Received 19 January 2010; revised 14 May 2010; accepted 21 June 2010; published 20 October 2010.

[1] We develop a technique for using monostatic, electronically steerable incoherent scatter radar (ISR) to generate 2-D estimates of  $F$  region flow fields. Tikhonov regularization is used to achieve robustness in the presence of spatial variation. The regularization functional imposes partial incompressibility on the medium and is therefore physically justified. Although the estimator has difficulty resolving sharp discontinuities, it performs well in regions of uniform flow. In order to characterize the effect of the regularization parameter, we test the performance of the operator in three simulated scenarios. We then analyze data from an experiment on the Poker Flat ISR. The experimental results are validated against coregistered all-sky optical data and are found to be mostly consistent with these independent measurements. Namely, the radar-derived estimates show a reduction of ion flow wherever the optical data indicates an auroral enhancement. The estimated flow is directed parallel to an arc boundary, consistent with an electric field directed toward the arc.

**Citation:** Butler, T. W., J. Semeter, C. J. Heinselman, and M. J. Nicolls (2010), Imaging  $F$  region drifts using monostatic phased-array incoherent scatter radar, *Radio Sci.*, 45, RS5013, doi:10.1029/2010RS004364.

### 1. Introduction

[2] The high-latitude ionosphere is subject to magnetospheric forcing in a variety of forms (e.g., magnetospheric precipitation, thermospheric winds, and Alfvén waves). These sources impart a high degree of variability on the density, composition, temperature, and flows of the ionized and neutral gases. Resolving this local variability is a particular interest of high-latitude atmospheric studies. In this paper, we develop an inverse-theoretic approach to estimating 2-D flow fields from line-of-sight velocities obtained from a monostatic electronically steerable radar antenna.

[3] Incoherent scatter radar (ISR) is a powerful technique for studying the structure of the ionosphere. In a monostatic ISR, the backscattered power spectrum is analyzed to provide range-resolved estimates of ionospheric state parameters. This work focuses on the bulk Doppler shift of the spectrum, which provides a measure of the bulk ion flow projected onto the line of sight of the radar beam. By

steering the radar to observe velocities in a number of directions, it is possible to reconstruct the components of the underlying vector velocity. Hagfors and Behnke [1974] first demonstrated the recovery of a single vector velocity using a scanning monostatic ISR. Doupnik *et al.* [1977] included a physical model of ionospheric velocity to estimate the electric field vector. Sulzer *et al.* [2005] introduced linear regularization to deal with rapid temporal variations.

[4] A notable limitation of this scanning mode is the inertia associated with physically steering a heavy dish. In recent years, ISR's employing electronically steerable arrays have begun to appear: notably, the Middle and Upper atmosphere (MU) radar in Japan, Poker Flat ISR (PFISR) in Alaska, the Resolute Bay ISR (RISR) in Canada, and the planned EISCAT 3D project. These systems overcome that inertial burden. An experiment can now be performed that probes the sky in multiple directions on a pulse-by-pulse basis. The coherent integration required to resolve plasma state parameters is performed, in essence, simultaneously over all directions, analogous to the way an image is formed in a CCD camera. Although there is an inherent trade-off between temporal and spatial resolution, this direct imaging modality has already yielded promising results [Semeter *et al.*, 2008; Nicolls and Heinselman, 2007a, 2007b]. Hysell *et al.* [2009] verify PFISR-derived velocity measurements by comparing with an interferometric imaging technique from a coherent scatter radar.

<sup>1</sup>Department of Electrical and Computer Engineering and Center for Space Physics, Boston University, Boston, Massachusetts, USA.

<sup>2</sup>SRI International, Menlo Park, California, USA.

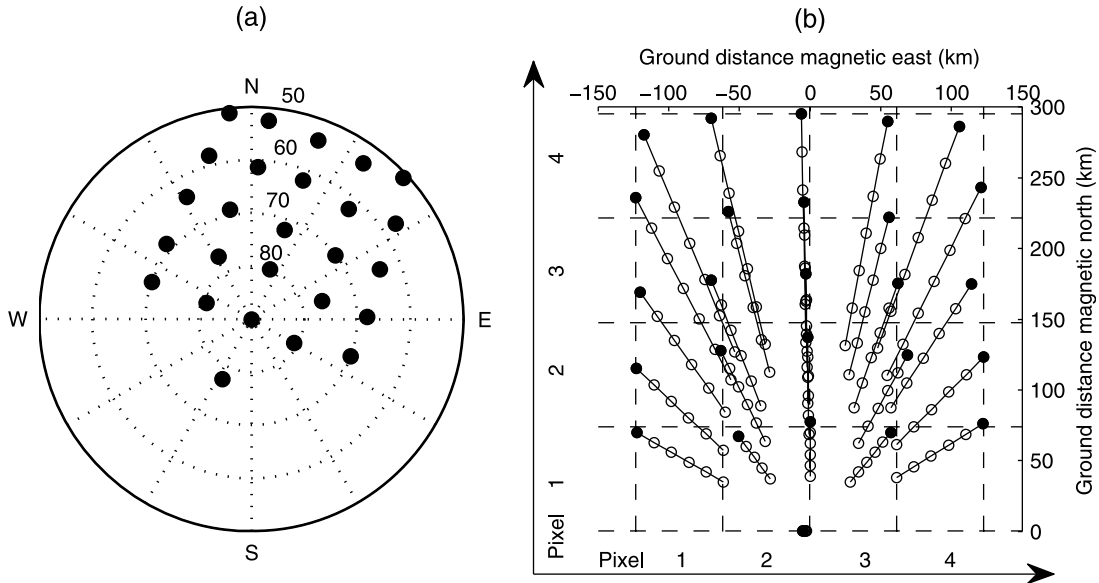


**Figure 1.** The beam configuration used in the experiment of section 3. (a) The 26 beams in angular coordinates. (b) Rotation of measurements and pixelization in radar-centered geomagnetic coordinates. Several samples are acquired along each beam, equally spaced in range. Solid circles denote the endpoints of each beam.

[5] Phased array radar experiments generally involve an arbitrary number and arrangement of beams. Thus the problem of estimating velocity components from projections is often overdetermined. *Heinselmann and Nicolls* [2008] employ a linear least squares estimator, which is capable of handling this type of problem (making use of all available data while respecting the limited rank of the corresponding projection operator). Our approach is similar, but we include physical constraints in the estimate (i.e., regularization) to deal with the spatial variability characteristic of high latitudes.

[6] We analyze the limitations of this type of reconstruction in the high-latitude  $F$  region and present a case study. In section 2, we describe the measurement process and how we exploit the rapid scanning capability of PFISR to generate a two-dimensional “snapshot” of  $F$  region ion flow patterns. The accuracy of the technique is evaluated through simulation in section 3. We also present a case study showing some of the features demonstrated in the preceding simulation. Section 4 presents a summary of findings and suggested extensions.

## 2. Methodology

[7] We frame the problem of velocity field estimation as a linear discrete inverse problem. That is, given a forward model mapping the underlying field  $\mathbf{v}(x, y)$  to a set of independent line-of-sight (LOS) measurements

$\mathbf{v}_{\text{los}}$ , we generate an estimate  $\hat{\mathbf{v}}(x, y)$  by running the process in reverse, i.e., by applying the inverse model.

### 2.1. Observation Geometry

[8] PFISR employs an electronically steerable array, which can be cycled through a predefined set of beam positions on a pulse-by-pulse basis. This allows sampling an entire field “simultaneously,” overcoming the time ambiguity introduced by the relatively slow scanning of a dish antenna. Measurements are resolved along range in each direction, so that scanning in both azimuth and elevation allows volumetrically distributed data to be resolved. One full cycle of measurements from all beams is defined as a “frame.”

[9] We focus on a beam pattern particular to a PFISR experiment on 24 March 2009. The volumetric data were acquired using a square array of  $5 \times 5$  beams with one additional beam in the up- $B$  direction (Figure 1a). At 350 km altitude, the sampled angular space subtends an approximately rectangular region of dimensions 300 km  $\times$  250 km. In Figure 1b, the entire set of sample points is projected to  $z = 0$ . We include data ranging in altitude from 200 to 350 km, where the parallel component of  $\mathbf{v}$  is considered to be negligible. Although significant ion upwelling may occur, field-aligned velocities in this range are  $< 200$  m/s, while convective flows are typically in the km/s range [*Fujii et al.*, 2002].

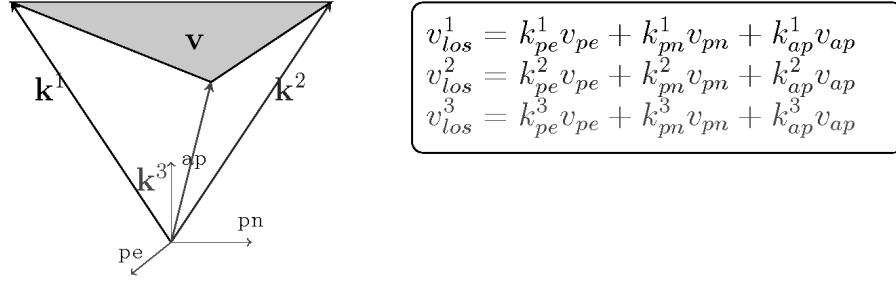


**Figure 2.** A uniform vector velocity is projected onto three lines of sight.

[10] After collecting a certain number of samples (determined by the desired temporal resolution as well as the signal statistics) along each beam in Figure 1, the auto-correlation function (ACF) is computed and analyzed to find the set of ISR parameters that best fits the data. A nonlinear least squares fitting procedure yields the line-of-sight velocity for each sample point.

## 2.2. Forward Model

[11] Each ACF yields an independent measurement of range-resolved  $v_{los}^i$ , the ion velocity projected along the direction of beam  $i$ . Consider the simplified example in Figure 2. The three measurements  $v_{los}^i$  are projections of the vector  $\mathbf{v} = [v_{pe}, v_{pn}, v_{ap}]^T$  (in geomagnetic coordinates, where the subscripts  $pe$ ,  $pn$ , and  $ap$  stand for perpendicular-east, perpendicular-north, and antiparallel components, respectively) onto three unique beam directions. This threefold projection is a linear operation, and can therefore be expressed in matrix form:

$$\underline{v}_{los} = \begin{bmatrix} v_{los}^1 \\ v_{los}^2 \\ v_{los}^3 \end{bmatrix} = \begin{bmatrix} k_{pe}^1 & k_{pn}^1 & k_{ap}^1 \\ k_{pe}^2 & k_{pn}^2 & k_{ap}^2 \\ k_{pe}^3 & k_{pn}^3 & k_{ap}^3 \end{bmatrix} \begin{bmatrix} v_{pe} \\ v_{pn} \\ v_{ap} \end{bmatrix} = \mathbf{A}\mathbf{v}, \quad (1)$$

where  $\mathbf{k}^i = [k_{pe}^i, k_{pn}^i, k_{ap}^i]^T$  is a unit vector in the direction of beam  $i$ . Ideally, this can be solved by inverting the square matrix  $\mathbf{A}$ . This is rarely practical, for reasons that will be treated later.

[12] In the example above, all the measurements correspond to the same velocity  $\mathbf{v}$ . Since we are interested in resolving the spatial variability of the vector field  $\mathbf{v}(x, y)$ , we do not assume uniformity among all the measurements in a given frame. Instead, the matrix  $\mathbf{A}$  must be expanded to include multiple, spatially distributed vectors  $\mathbf{v}(x, y)$ . Already, we run up against a limitation of algebraically inverting the projection operation, since this expanded  $\mathbf{A}$  is not necessarily a full-rank matrix.

## 2.3. Discretization

[13] Although the LOS measurements are inherently discrete, we assume an underlying continuous velocity field  $\mathbf{v}(x, y)$ . For implementation in a computer, this can be discretized spatially and regarded as a column vector, i.e.,

$$\mathbf{v}(x, y) = \sum_{j=1}^N \mathbf{v}_j b_j(x, y),$$

where  $\{b_j(x, y)\}_{j=1 \dots N}$  is some basis spanning the region of interest. This can be simple rectangular pixels, or something more elaborate such as a multiscale (wavelet) basis. In practice, each component of the vector  $\mathbf{v}$  is discretized independently, and the resulting column vectors stacked so that

$$\underline{\mathbf{v}} = \left[ v_{pe}^1, \dots, v_{pe}^N, v_{pn}^1, \dots, v_{pn}^N, v_{ap}^1, \dots, v_{ap}^N \right]^T.$$

[14] We use a rectangular pixel basis because it is intuitive and easy to implement. It also allows an arbitrary beam arrangement. Because the beams in Figure 1a are roughly aligned with the magnetic meridian, the data is first rotated to geomagnetic coordinates so that the data are aligned with pixels. The  $4 \times 4$  pixelization of Figure 1b satisfies a trade-off between spatial resolution and the amount of independent information contained in each pixel. Although we could choose a finer sampling, each pixel must contain data from approximately three beams.

[15] In general, the velocity field  $\mathbf{v}(x, y)$  is divided into  $N$  pixels and we observe  $M$  LOS projections. This set of projections is expressed in the  $M \times 3N$  matrix

$$\mathbf{A} = \left[ \begin{array}{ccc|ccc|ccc} k_{pe}^1 & \dots & \dots & k_{pn}^1 & \dots & \dots & k_{ap}^1 & \dots & \dots \\ \dots & k_{pe}^2 & \dots & \dots & k_{pn}^2 & \dots & \dots & k_{ap}^2 & \dots \\ \vdots & & & \vdots & & & \vdots & & \\ \dots & \dots & k_{pe}^M & \dots & \dots & k_{pn}^M & \dots & \dots & k_{ap}^M \end{array} \right].$$

That is, each row contains three nonzero elements mapping the velocity vector in the  $j$ th pixel to the  $i$ th LOS measurement such that (by extension of (1))

$$\underline{v}_{\text{los}} = \mathbf{A}\underline{v}. \quad (2)$$

Clearly, for an arbitrary discretization and selection of beams, this matrix is not directly invertible. Moore-Penrose pseudoinverse and least squares fitting may yield a solution to (2), but such solutions do not consider statistical uncertainty in the data. Furthermore it is useful to constrain the solution according to a spatial regularity criterion. We therefore turn to the field of inverse theory.

## 2.4. Inversion

[16] Inverse theory provides a framework for introducing exogenous information to solve undetermined and overdetermined problems. Inverse theory is discussed in a number of standard texts [e.g., *Tarantola, 2005; Menke, 1989; Aster et al., 2005*]. The forward model (2) consists of three terms: the LOS observations  $\underline{v}_{\text{los}}$ , the underlying discretized velocity field  $\underline{v}$ , and the operator  $\mathbf{A}$  mapping one to the other. An inverse model is constructed from these three elements and then applied to the observations to recover the underlying field. Several approaches have been developed, and we proceed with the classic method of Tikhonov regularization.

[17] In general terms, a linear inverse problem considers a set of observations  $\mathbf{y}$  corresponding to the state  $\mathbf{x}$  through the linear formula  $\mathbf{y} = \mathbf{A}\mathbf{x}$ . The goal is to estimate  $\mathbf{x}$  by minimizing a function of the observations, usually paired with a side constraint on the estimate, for example:

$$\hat{\mathbf{x}} = \arg \min_{\mathbf{x}} \left( \|\mathbf{y} - \mathbf{A}\mathbf{x}\|_{\mathbf{W}_1}^2 + \alpha^2 \|\mathbf{L}\mathbf{x}\|_{\mathbf{W}_2}^2 \right). \quad (3)$$

The first term in parentheses is a data fit term, the second is the side constraint, and  $\alpha$  is the regularization parameter controlling the relative influence of each term. The notation  $\|\cdot\|_{\mathbf{W}}$  denotes a weighted  $l^2$  norm:  $(\cdot)^T \mathbf{W}(\cdot)$ . The solution of (3) is given by the normal equations

$$(\mathbf{A}^T \mathbf{W}_1 \mathbf{A} + \alpha^2 \mathbf{L}^T \mathbf{W}_2 \mathbf{L}) \hat{\mathbf{x}} = \mathbf{A}^T \mathbf{W}_1 \mathbf{y}. \quad (4)$$

[18] This is the deterministic view of inverse theory and regularization. We can further derive the solution by making use of the statistics of each quantity. Let us assume that  $\mathbf{y}$  is corrupted by a zero mean noise vector  $\mathbf{w}$ ,

$$\mathbf{y} = \mathbf{A}\mathbf{x} + \mathbf{w},$$

where  $\mathbf{x}$  is a zero-mean Gaussian random variable with covariance matrix  $\mathbf{Q} = (\alpha^2 \mathbf{L}^T \mathbf{W}_2 \mathbf{L})^{-1}$ ,  $\mathbf{w}$  is Gaussian with covariance matrix  $\mathbf{R} = \mathbf{W}_1^{-1}$ , and  $\mathbf{w}$  and  $\mathbf{x}$  are uncorrelated.

Then, rearranging terms and using Bayes' rule, (3) is equivalent to

$$\begin{aligned} \hat{\mathbf{x}} &= \arg \max_{\mathbf{x}} \left( -\frac{1}{2} \|\mathbf{y} - \mathbf{A}\mathbf{x}\|_{\mathbf{R}^{-1}}^2 - \frac{1}{2} \|\mathbf{x}\|_{\mathbf{Q}^{-1}}^2 \right) \\ &= \arg \max_{\mathbf{x}} [\ln p(\mathbf{y}|\mathbf{x}) + \ln p(\mathbf{x})] \\ &= \arg \max_{\mathbf{x}} \ln p(\mathbf{x}|\mathbf{y}). \end{aligned}$$

That is, (4) is the maximum a posteriori (MAP) estimator with a side constraint imposed on  $\mathbf{x}$ . Given these statistics, the error covariance can also be determined. In summary, the estimate is given by

$$\hat{\mathbf{x}}_{\text{MAP}} = (\mathbf{A}^T \mathbf{R}^{-1} \mathbf{A} + \mathbf{Q}^{-1})^{-1} \mathbf{A}^T \mathbf{R}^{-1} \mathbf{y}, \quad (5)$$

and the error covariance is

$$\Sigma_{\hat{\mathbf{x}}} = (\mathbf{A}^T \mathbf{R}^{-1} \mathbf{A} + \mathbf{Q}^{-1})^{-1}. \quad (6)$$

[19] So far, the discussion has been in very general terms, with the side constraint  $\|\mathbf{L}\mathbf{x}\|^2$  unqualified. Typically, this constraint is chosen to penalize large values ( $L = I$ ) or to enforce smoothness ( $L$  represents some discrete approximation to the first derivative). For the problem of recovering ion flow, we argue that the appropriate constraint should represent the divergence operator. That is, the ionosphere is incompressible, and we may apply this physical constraint ( $\nabla \cdot \mathbf{v} = 0$ ) to regularize the inversion. The matrix corresponding to the divergence operation is

$$\mathbf{L} = \begin{bmatrix} L_{pe} & 0 & 0 \\ 0 & L_{pn} & 0 \\ 0 & 0 & L_{ap} \end{bmatrix}, \quad (7)$$

where the submatrices encode the discrete approximations of the first derivatives, e.g.,

$$L_{pn} = \begin{bmatrix} -1 & 1 & 0 & 0 & 0 & \dots & 0 \\ 0 & -1 & 1 & 0 & 0 & \dots & 0 \\ & & & \ddots & & & \\ 0 & \dots & 0 & 0 & -1 & 1 & 0 \\ 0 & \dots & 0 & 0 & 0 & -1 & 1 \\ 0 & 0 & 0 & \dots & 0 & 0 & 0 \end{bmatrix}.$$

Because the forward difference generates a shorter vector than its input, each submatrix has some all-zero rows. This makes the matrix  $\mathbf{Q}$  degenerate; it has some zero eigenvalues corresponding to the boundaries. The boundary conditions need not be included in (5) since the data-fit term will select values from the observations. The smoothness constraint is only enforced for the perpendicular components. Since we expect the field-aligned component to be

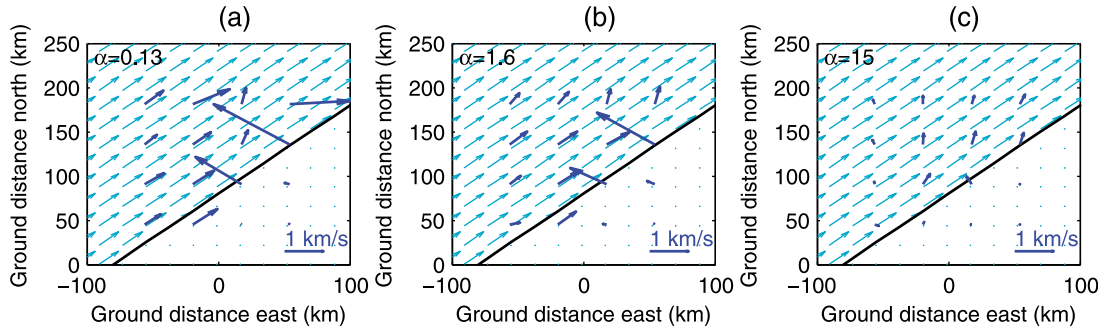


**Figure 3.** Method A (field magnitude constraint). Estimates of the simulated velocity field for three values of  $\alpha$ .

very small, we impose a constraint on the magnitude of this component rather than its smoothness, i.e.,  $L_{ap} = I$ .

### 3. Results

[20] The regularization parameter  $\alpha$  is a nonnegative factor that balances the relative influence of measured data and a priori information. Before applying the estimator to experimental data, it is important to evaluate how  $\alpha$  affects the result. The “optimal” value of  $\alpha$  is difficult to define since selection of the regularization parameter is typically a subjective process. A single value is not likely to yield subjectively “optimal” results for all measurements. Nevertheless, iterative methods of selection, whether semiobjective or utterly subjective (e.g., visual inspection), in a controlled simulation can aid in finding a useful practical range of  $\alpha$ .

[21] In the following sections, we examine the effect of the incompressible flow constraint by comparing two estimators that differ only in the matrix  $L$ : Method A uses  $L = I$ ; Method B uses the  $L$  given by (7). Note that in (5) and (6), the side constraint  $L$  is absorbed into the covariance matrix  $Q$ . When  $L = I$ ,  $Q$  differs from  $W_2^{-1}$  only by a scalar factor. Hence the interior weighting matrix  $W_2^{-1}$  for the side constraint is itself a (diagonal) covariance matrix that encodes the respective variabilities of  $v_{pe}$ ,  $v_{pn}$ , and  $v_{ap}$ , which we have arbitrarily chosen as  $\sigma_{pe} = \sigma_{pn} = 500$  m/s,  $\sigma_{ap} = 15$  m/s.  $R$ , the error covariance, is a diagonal matrix with variances inversely proportional to range squared, and with a scaling factor chosen so that the standard deviation is 10 m/s at 100 km.

#### 3.1. Simulation

[22] We begin by simulating a velocity field morphology that is common during a substorm, namely, a flow shear along an active auroral boundary. The light-colored arrows in Figure 3 represent the “ground truth” horizontal flows. The field pattern is divided into two regions: zero flow and

uniform flow. The thick diagonal line signifies the boundary of the two regions. This pattern is motivated by auroral observations [de la Beaujardière et al., 1977; de la Beaujardière and Vondrak, 1982; Weber et al., 1991; Bahcivan et al., 2006]. Within an auroral arc is a region of enhanced density (thus conductivity). The electric field responds to this enhancement by dropping significantly, and therefore the ion drift goes to essentially zero. At the arc boundary, the potential gradient produces an electric field such that the ion flow is parallel to the boundary. The drop in the electric field is quite abrupt, and for the resolution considered here the step function between the two regions is an appropriate approximation.

[23] The LOS measurements are generated from this simulated field  $\mathbf{v}$  via (2) and then perturbed by a zero-mean Gaussian noise vector  $\mathbf{e}_{\text{los}}$  with covariance  $R$  as described above. The three fields shown in Figure 3 are estimated using Method A and different values of the regularization parameter  $\alpha$ . Figure 4 shows the corresponding simulation for Method B. In general, both estimators have difficulty resolving the discontinuity (a violation of the assumption of uniformity within each pixel). For small  $\alpha$ , both produce very similar solutions (as  $\alpha$  approaches zero, the estimators are equivalent). As  $\alpha$  increases, the respective side constraints come into play. In Figure 3, the preferred solution has the minimum overall magnitude, while in Figure 4, the solution exhibits smooth transitions between neighboring pixels.

[24] The performance of the estimators is shown more comprehensively in Figures 5 and 6, which plot the bias and standard deviation of both estimators as a function of  $\alpha$ . The text above each plot indicates the pixel (see Figure 1b). The radar is located at the bottom, between the two center pixels ((2,1) and (3,1)). The performance of the inversion is highly dependent on the geometry (i.e., the LOS direction vectors in row (pixel)  $j$  of  $A$ ). Inversion demands that the direction cosines be dissimilar. Otherwise, not enough independent information is present to recover the cross-range component.

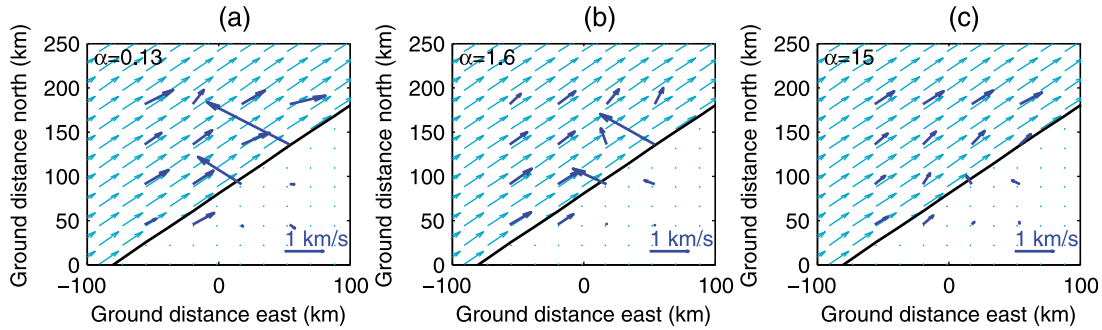


**Figure 4.** Method B (incompressible flow constraint). Estimates of the simulated velocity field for three values of  $\alpha$ .

[25] In each plot, the three velocity components are represented by different colored/styled lines (see legend). The bias and standard deviation are computed via Monte Carlo simulation. In both cases, the field-parallel bias (red) is essentially zero, regardless of  $\alpha$ . The exception is in pixels (3,2) and (4,3), which fall on the discontinuity (see Figure 3). For low  $\alpha$  both estimators handle this violation of the uniformity assumption by estimating a very large field-parallel component. There is a significant southward bias (green) in pixel (3,4) in Method A that is not present in Method B. For  $\alpha > 2$ , Method B exhibits more bias in the zero-flow region. This is particular to the phantom velocity field and results from the divergence operator's wider support. Method A resolves the zero region better, but this is because it favors the zero solution. In the nonzero region, the solution is very poor (see Figure 3c). In general, we see the trend that as more regularization is applied ( $\alpha$  increases), the standard deviation of the estimator decreases while bias increases. Compared to Method A, in regions of uniform flow (farther from the discontinuity, e.g., pixel (3,4)), Method B reduces bias at the expense of error variance.

[26] The above discussion addresses the estimates in each pixel separately, but not the correlations between pixels. Figure 7 shows error ellipses for Methods A and B and regularization parameter value  $\alpha = 15$ . The width of the ellipse indicates the variance of the estimator in each component (only horizontal components  $pe$  and  $pn$  are considered). The eccentricity indicates that one component is better represented by the measurements. The angle indicates correlation between the two errors and is roughly aligned such that the error in the transverse direction is greater than the line-of-sight component. The semiminor axis generally points toward the radar (i.e., the line-of-sight component is better represented by the data), while the semimajor axis indicates less accuracy in estimating the

transverse component. Although both the measurements and noise are uncorrelated, the estimates (and therefore the errors) become correlated through the inversion operation. As before, the performance is geometry-dependent: those estimates farthest from the radar (top row) incur the largest errors for two reasons: first due to the range dependence of  $R$ , second since fewer samples fall within these pixels (see Figure 1b). The semimajor axis is wider for Method B (solid lines) because of its wider support; the error covariance is greater because the estimate in each pixel is constrained by local measurements as well as data from its neighbors.

[27] Figure 8 shows the L curves for this simulation. The L curve is a semiquantitative strategy for selecting an optimal level of regularization. The vertical axis is a measure of the side constraint (in this case the  $L^2$ -norm of the divergence of  $\hat{\mathbf{v}}$ ). The horizontal axis is a measure of how well the estimate fits the data. The curve is plotted for a range of  $\alpha$  to characterize the trade-off between smoothness (vertical axis) and data fit (horizontal). Closer to the origin is better. This curve typically takes the shape of the letter "L." The vertical segment corresponds to low  $\alpha$ , where data fit takes priority over smoothness. In this regime, increasing  $\alpha$  results in a smoother estimate that is still consistent with the data. In the horizontal segment,  $\alpha$  has less effect on the smoothness of the solution but results in an ever more inconsistent estimate. The "optimal"  $\alpha$  lies between these two extremes, at the knee of the curve if such a point can be identified.

[28] The smoothness metric in Figure 8 for a given  $\alpha$  is lower (i.e., better) for Method B while the data fit is consistently better. The knee of the curve is more easily identifiable for Method A at  $\alpha \approx 15$ . This value is later used in comparisons to make qualitative assessments of estimator performance versus  $\alpha$ .

**Figure 5.** Effect of varying the regularization parameter  $\alpha$ , Method A: (a) bias and (b) standard deviation. Thin lines represent the diagonal elements of (6).

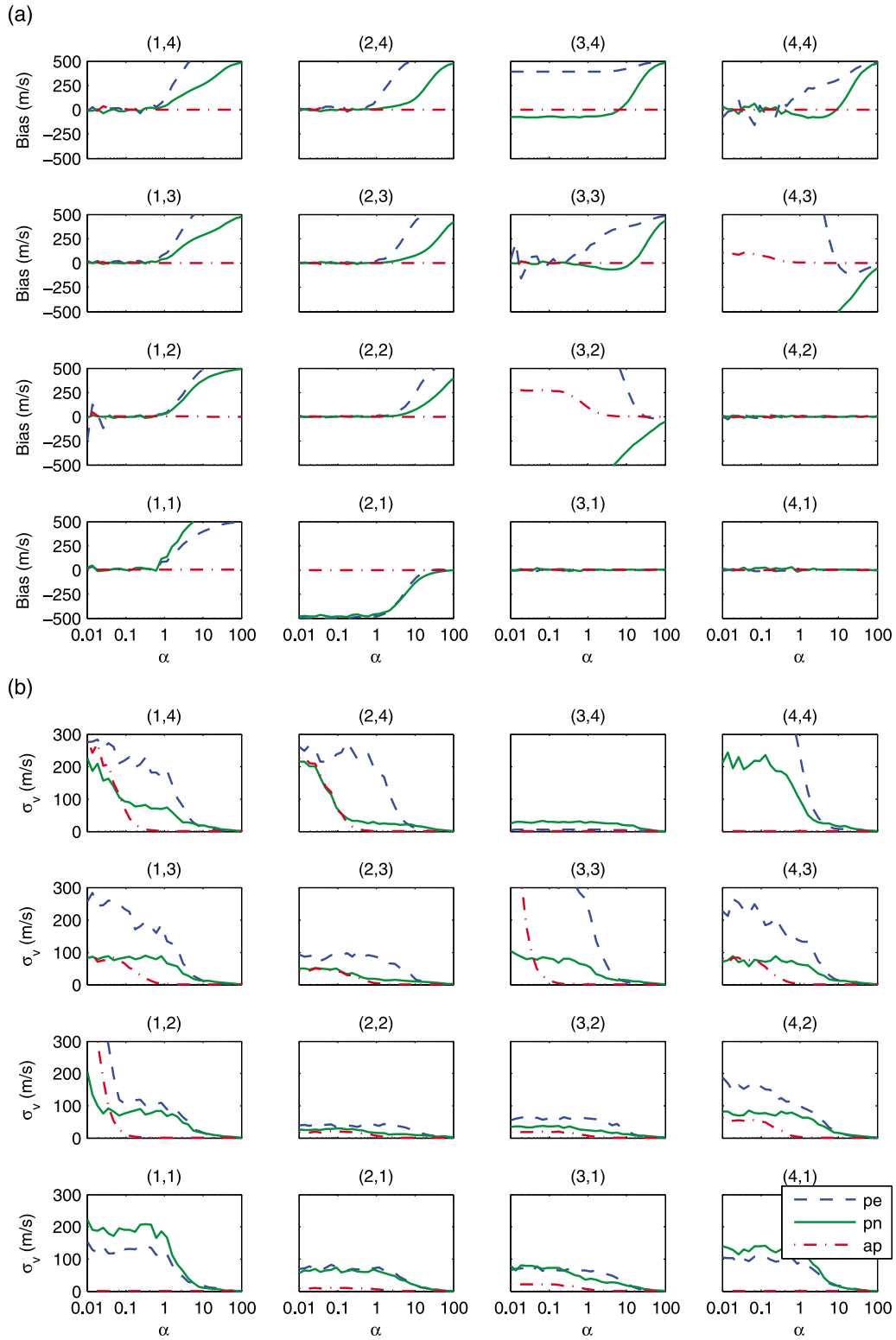


Figure 5

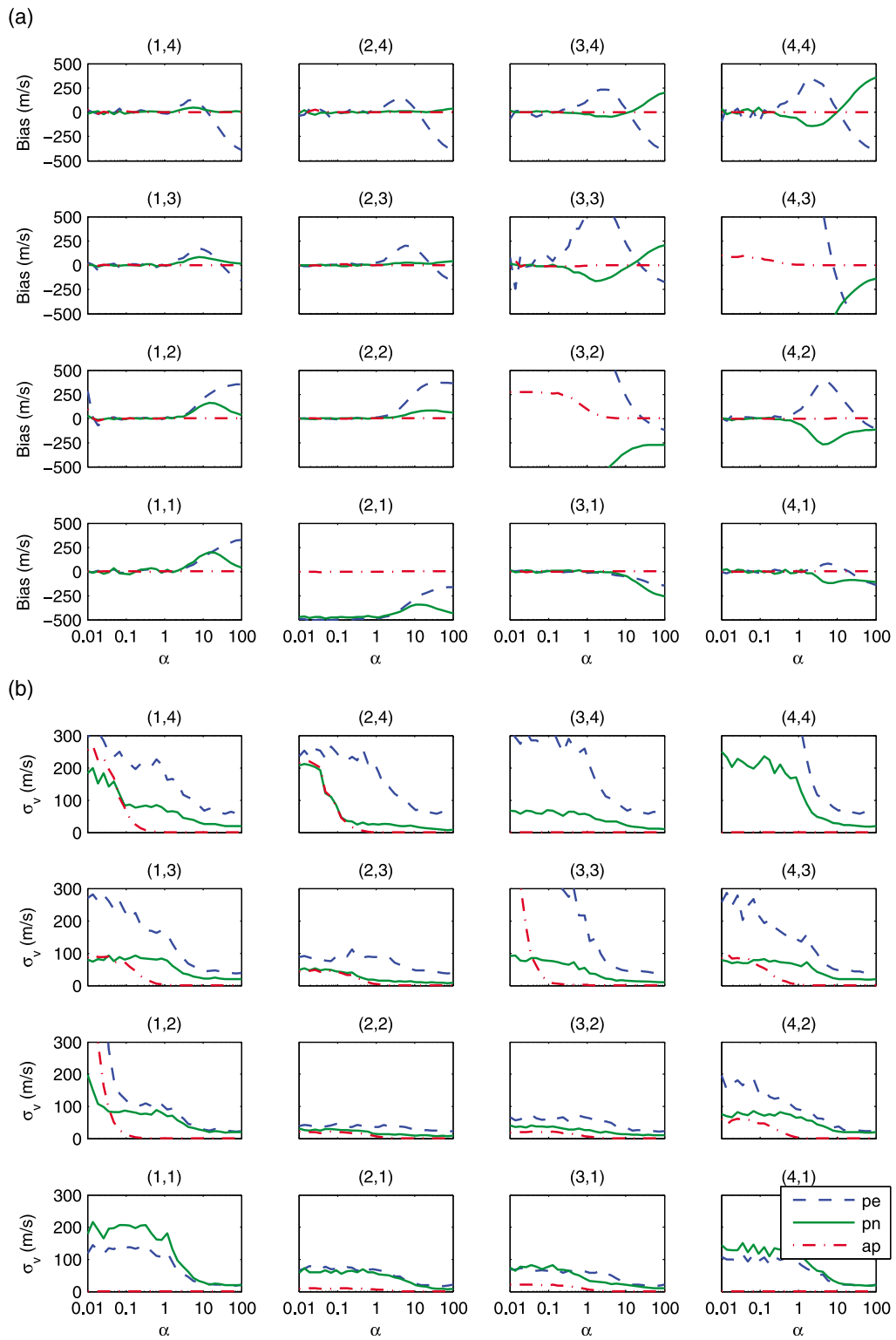
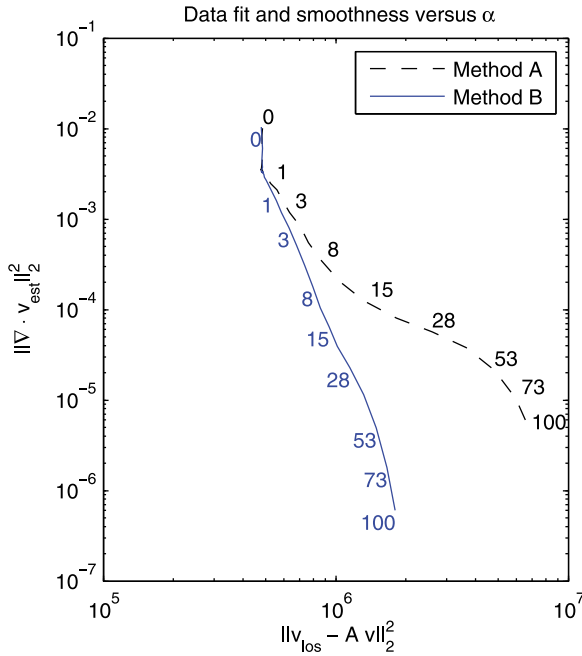


Figure 6



**Figure 7.** The  $1 - \sigma$  error ellipses. Dashed lines give the error for Method A. Solid lines give the error for Method B. The units are m/s.

[29] In the discussion above we justified using the field shown in Figures 3 and 4. This was motivated by a particular phenomenon that is expected to occur in the ionosphere during substorms. The advantage of spatial regularization is that it provides robustness in the presence of spatial variation. Hence we now consider two variations of the earlier pattern: a uniform field  $\mathbf{v}(x, y) \equiv \mathbf{v}$  (see Figure 9) and a very thin enhancement with oppositely directed velocity on the other side of the arc (see Figure 10). Figures 9b and 9c and Figures 10b and 10c (Figures 9d and 9e and Figures 10d and 10e) show a pair of estimates using Method A (Method B) for both low and high values of  $\alpha$ .

[30] Figures 9a and 10a show the L curves for each of these cases. Some general observations can be made pertaining to both cases. As before, Method A reaches a point of diminishing returns when it begins to emphasize smallness over data fit. The L curve levels to horizontal and the estimated field approaches zero. By comparison, the L curve for Method B is closer to the origin for all values of  $\alpha$ .

[31] The uniform field (Figure 9) presents no challenge for either estimator, since this is an important assumption

in its design. But when the regularization “kicks in,” Method A defeats itself by approaching the zero field. Perhaps more importantly, the “shrinking” in Method A dramatically alters the direction and overall shape of the flow pattern. It is this overemphasis of the side constraint that leads to the horizontal segment of the L curve. By comparison, Method B preserves the uniform direction of  $\hat{\mathbf{v}}$  for all  $\alpha$ , and the L curve is practically vertical.

[32] Turning now to the shear flow case (Figure 10), the discontinuity is even more difficult to resolve than the step function considered previously. Though reconstruction errors do extend beyond the position of the discontinuity (again due to the relatively wide support of the divergence operator), both methods perform best where the underlying field matches the assumption of uniformity. In particular, the top row of estimates is nearly perfect. Around  $\alpha = 15$  (Figure 10e), Method B comes closest to the true field. For higher values (not shown), the solution begins to approach something like solenoidal flow (i.e., the ideal solution if  $\nabla \cdot \mathbf{v} = 0$  exactly). Hence the knee (albeit slight) located around  $\alpha = 15$  in Figure 10a. The differences in the L curves for this case are not as dramatic, but the same general observations apply: Method B performs better, i.e., it is consistently both smoother and a better fit to the observed data.

### 3.2. Case Study: 24 March 2009

[33] In an experiment run 24 March 2009, PFISR was operated in the 26-beam mode of Figure 1a. The full array of 26 beams (“frame”) was sampled every 5.5 s, during which time returns from 14 uncoded 480  $\mu$ s pulses were acquired in each direction on each of two interleaved frequency channels. The auroral activity of this night generated returns with high SNR, allowing estimates of LOS velocities from few samples.

[34] The results described in this section were obtained during a 1 h period using integrations of 30 s, corresponding to  $\sim 140$  pulses per beam. Values for the diagonal matrix  $R$  were supplied by the same the nonlinear fitter that generated the LOS estimates. The velocity fields were constructed using Method B with a regularization parameter of  $\alpha = 5$ . This value was chosen based on trial and error. Although the step function in the above simulations was considered realistic, it is an idealized “high-pass” phenomenon that rarely occurs exactly as presented. So it is more prudent to “tune” the estimator to emphasize data fidelity (i.e., lower  $\alpha$ ) rather than to risk oversmoothing.

[35] The estimated velocity fields were superimposed on optical images captured by a collocated digital all-sky camera. The camera captured both 557.7 nm and 630 nm wavelengths, but only the 557.7 nm data is displayed in

**Figure 6.** Effect of varying the regularization parameter  $\alpha$ , Method B: (a) bias and (b) standard deviation. Thin lines represent the diagonal elements of (6).

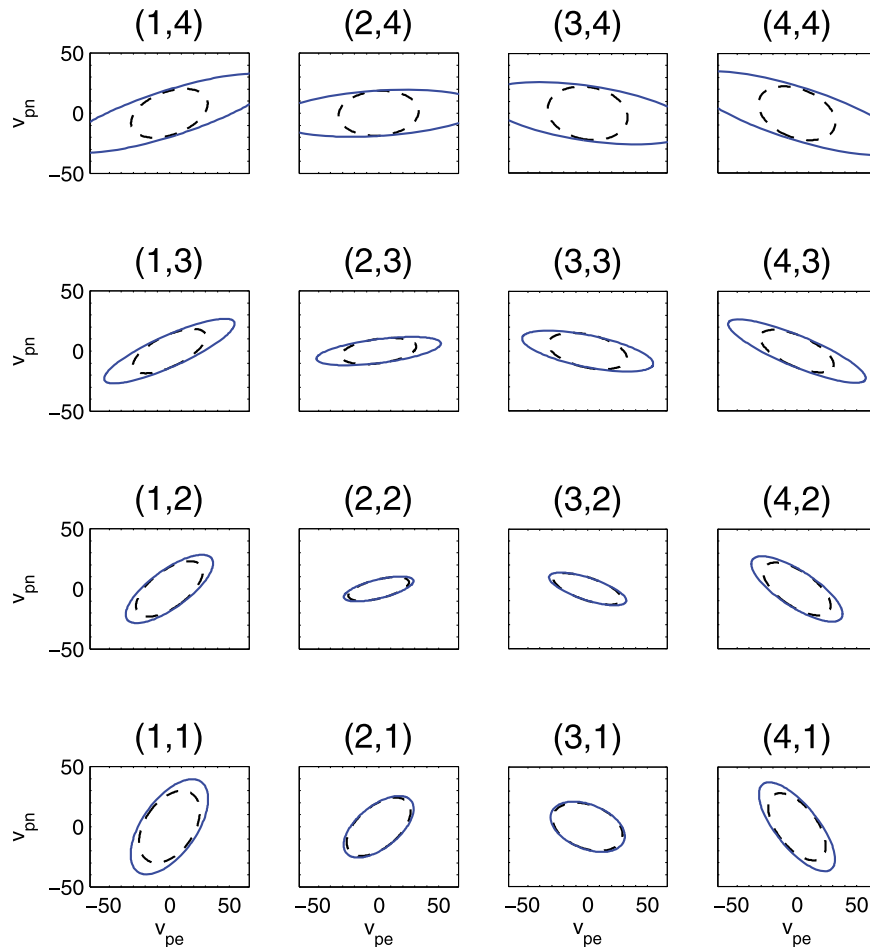


**Figure 8.** L curves for Methods A and B for the ground truth (cyan) velocity field pattern in Figures 3 and 4. Data fit metric is on the horizontal axis. Smoothness metric is on the vertical axis.

Figures 11–13. At a cadence of 20 s, the all-sky imager captures dynamics with timescales comparable to those captured by the radar reconstructions. The velocity fields and auroral images were coregistered assuming an auroral emission altitude of 120 km.

[36] Figure 11 shows 4 contiguous 30 s flow fields estimated in the vicinity of a stable east-west aligned arc of  $\sim 50$  km width. Figure 11a shows a relatively uniform flow in the magnetic westward direction, tangential to the arc boundary. There is a reduction in the velocity magnitude within the arc, consistent with a reduced electric field within the region of increased conductivity. Figures 11b and 11c depict the development of a flow reversal near the poleward boundary of the arc. The circulatory appearance of the flow field is reminiscent of Figure 10c. It is most likely an artifact of applying regularization to a flow shear extending beyond the region of observation.

The actual flow shear is probably similar to the phantom flow field in Figure 10. In Figure 11d, the uniform westward flow is recovered. Figure 12 gives a second example of a rapid ( $<30$  s) development of a large flow shear in the vicinity of a preexisting auroral form. In this case, the morphology is clearly undersampled in time, as the reversal appears only in Figure 12b.

[37] Such rapid fluctuations were commonly observed throughout this observing period. Figure 13 shows a longer sequence of 30 s flow fields during a period of somewhat more dynamic auroral activity. Although the correlation with auroral boundaries is less clear, we again see large fluctuations in both magnitude and direction of flow, as well as the ephemeral appearance of strong flow shears, throughout. Rapid localized fluctuations in convective flow have been identified by *Bristow* [2008] using the SuperDARN HF radar network. Their cause

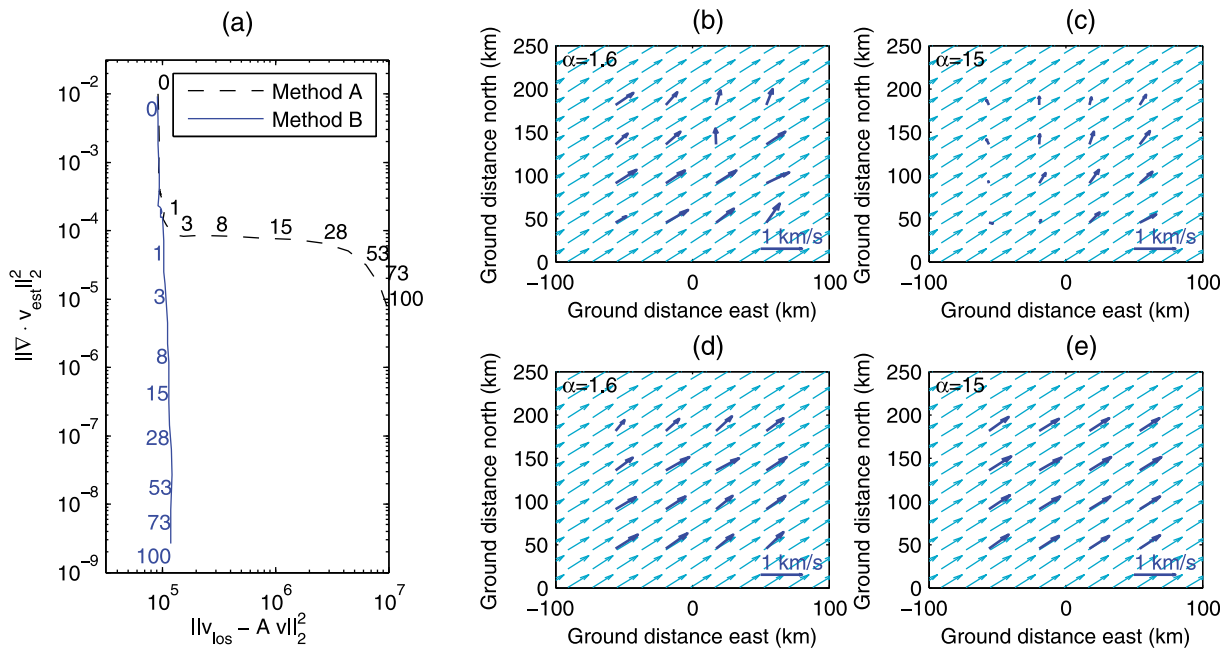


**Figure 9.** Uniform flow field. (a) L curve for Methods A and B. Sample reconstructions for both methods are shown: (b and c) Method A and (d and e) Method B.

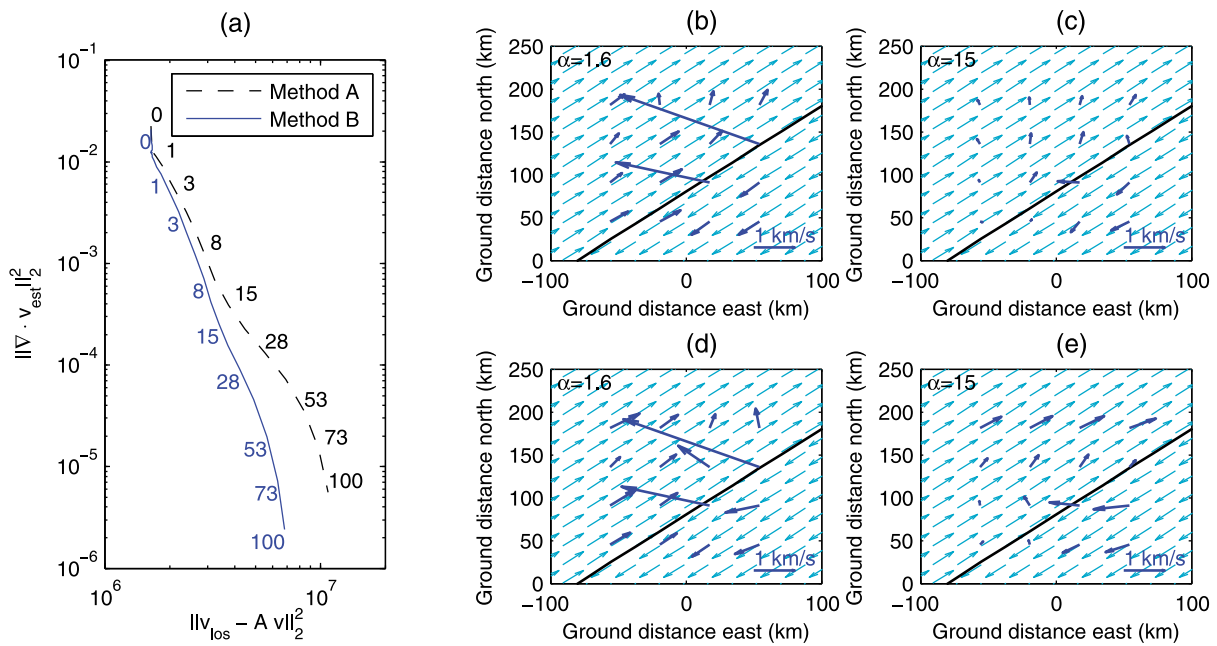


**Figure 10.** Shear with field reversal. (a) L curve for Methods A and B. Sample reconstructions for both methods are shown: (b and c) Method A and (d and e) Method B.

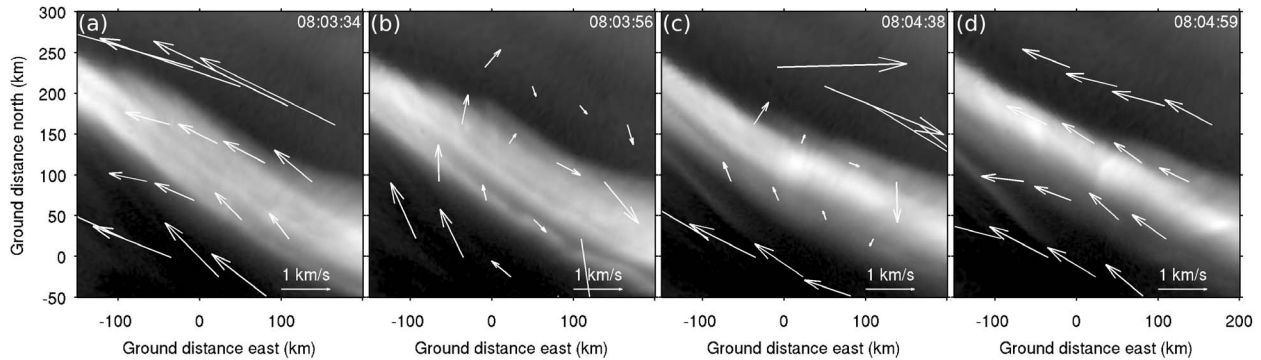


**Figure 11.** Coregistered ion convective flow fields and auroral forms constructed at 30 s cadence. Figures 11b and 11c illustrate the formation of a transient region of reversed flow near the poleward boundary of the arc.

remains unclear, and will be the subject of future work with these measurements.

#### 4. Discussion

[38] We have demonstrated the capability of an electronically steerable ISR to resolve  $F$  region flow fields. In order to achieve robustness in the presence of spatial variation, we chose to implement regularization in the solution. In our analysis we compared the performance of two regularization functionals: Method A, with a penalty on large-magnitude solutions, and Method B, the “incompressible flow” estimator with a penalty on local spatial variability.

[39] Both estimators have trouble resolving a sharp discontinuity, such as that seen in the simulation of section 3.1 (Figures 3 and 4). Both perform well in regions of uniform flow, with Method B having a slight advantage (Figure 6a, pixel (3,4)). For large values of the regularization parameter  $\alpha$ , Method A invariably approaches the zero field and

dramatically alters the general “shape” of the solution. Method B enforces uniformity (locally) or approaches the solenoidal solution (globally). Whether or not these solutions are realistic depends on the spatial variability of the process under observation. It is crucial to consider the effect of the regularization parameter  $\alpha$  on the analysis, whether it causes oversmoothing (Figure 10e), and whether artifacts appear as a result of the violated assumption of uniformity (Figures 10b and 10d).

[40] The accuracy of the velocity reconstruction depends heavily on the geometry of the problem. Hence each pixel is characterized by a unique error profile. See Figures 5–7.

[41] In applying the estimation technique to PFISR measurements, we validated our findings by comparing to a sequence of coregistered all-sky optical images from the same night. The optical data were captured at a similar timescale to the radar integration time, so the dynamics observed have a similar time resolution. The most important features of these data are the reduction of convective flow within an auroral enhancement [*de la Beaujardière and*

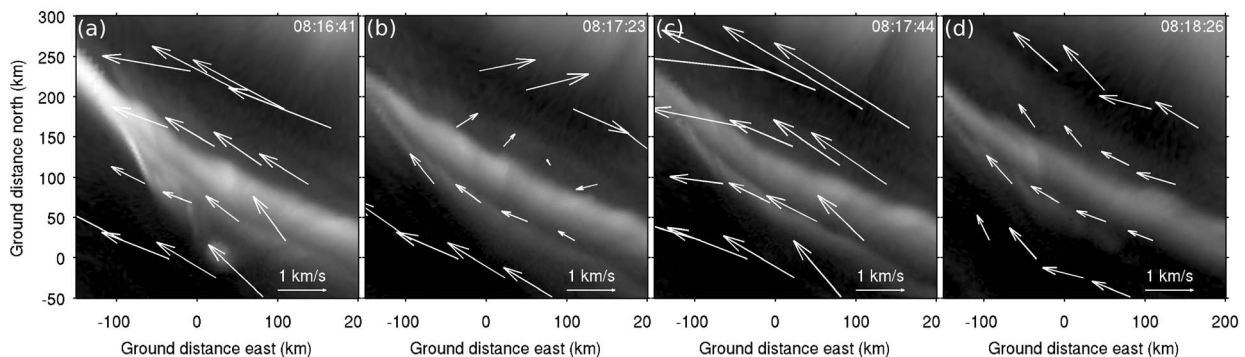


**Figure 12.** Another example similar to Figure 11.

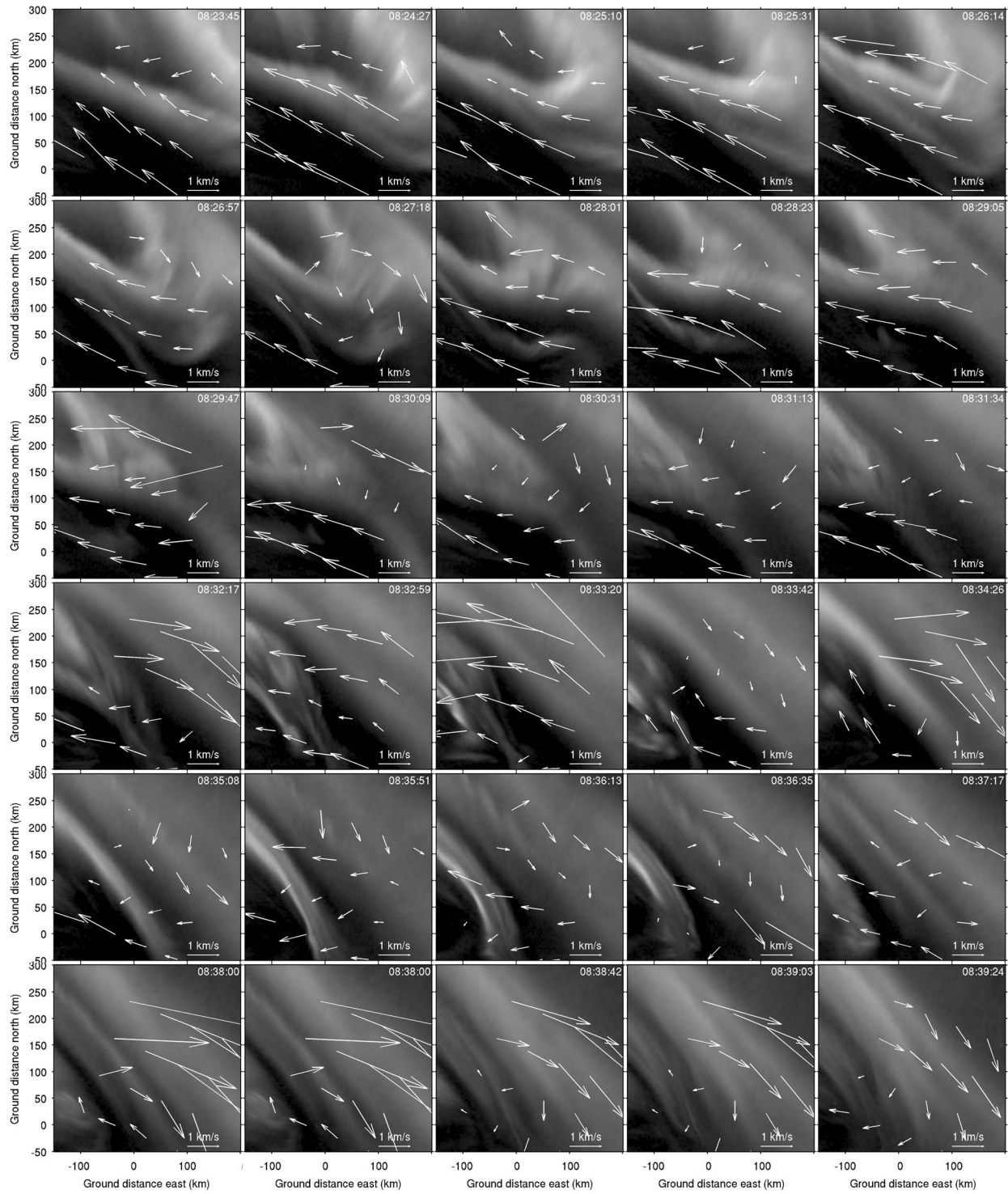


Figure 13. A longer sequence illustrating the relationship between flows and auroral forms.

Vondrak, 1982] and the convection's being generally parallel to the arc boundary, consistent with an electric field directed toward the arc [e.g., Lanchester et al., 1996].

[42] The Tikhonov formulation adopted above is advantageous for a variety of reasons. It is capable of handling the overdetermined problem. A smoothness constraint may be introduced by penalizing large local differences in the solution. Through the covariance matrix, the estimator accounts for the uncertainty inherent to all practical measurements. If something is known about the statistics of both the data and the prior model, the estimator also provides a measure of uncertainty in the form of the covariance matrix  $\Sigma_{\hat{x}}$ .

[43] To emphasize the novelty of this approach, it is worth comparing the acquisition and estimation procedure presented here to another method capable of estimating three dimensional  $F$  region ion convection. The tristatic EISCAT system receives three independent line-of-sight projections of ion flow velocity within a common volume. This allows unambiguous recovery of all three velocity components within the volume. PFISR is a monostatic radar, and the recovery of vector velocity requires the combination of neighboring measurements as described above. Although EISCAT is routinely operated in a meridional scanning mode that provides estimates along latitude, PFISR's electronic steerability allows acquisition of a "snapshot" as described in section 1. The monostatic arrangement is inherently unable to resolve the full flow vector due to the limited amount of independent information provided by neighboring measurements. The only way to resolve this ambiguity is by introducing outside information. The Tikhonov method of regularization is a natural way to incorporate such information.

[44] Exogenous information may come in the form of a physical model, e.g., a statistical model [Sulzer et al., 2005; Hysell et al., 2009]. It may also include ancillary data from separate instruments (i.e., sensor fusion). For instance, if there is a reason to believe the direction of ion flow is dominated by large-scale convection (e.g., if SuperDARN measurements indicate such a large-scale flow), the solution can be "steered" to a preferred direction to make use of this assumption. The solution is encoded with a directional preference by designing the a priori covariance matrix  $Q$  such that the horizontal variabilities  $\sigma_{pe}^2$  and  $\sigma_{pn}^2$  reflect confidence in the estimate of the respective components.

[45] In this work, we have used coregistered optical images to provide a context for interpreting the results. The optical brightness serves as a proxy for conductivity. Wherever an auroral arc occurs, the conductivity is higher. In order to maintain current continuity, the electric field in this region (and thus the drift velocity) is reduced. After identifying the arc boundary in the optical data, this can be used by the estimator to segment the solution into regions with different prior constraints. For instance,

since we expect the plasma flow at the boundary of an auroral arc to be parallel to the arc, we may tune the prior model to steer the solution in the appropriate direction. Rather than to perform this tuning by hand for each image, such contextual information could be provided to the estimator and automatically applied to its results.

[46] A notable feature of Figures 5 and 6 is the spatial inhomogeneity of the error covariance. This is unavoidable due to the poorly sampled nature of the pixelization in Figure 1b. That is, the measurement sample points are determined by the radar geometry, and we have laid a uniform  $4 \times 4$  grid over these sample points. As a result, some pixels contain more measurements (i.e., better statistics) than others. The velocity estimates in those pixels are more reliable than the poorly sampled top row of pixels. A nonrectangular basis expansion in the discretization may resolve this statistical variability.

[47] Even when the pixelization accommodates the radar geometry, the assumption of uniformity within each pixel is in opposition to the goal of resolving spatial variability. The optics-assisted segmentation mentioned above is an example of adaptive pixelization. In the simulation in section 3.1, the optimal pixelization would be two triangular pixels separated by the boundary indicated in Figures 3 and 4. A single velocity estimate is recovered for each pixel using all the measurements within that pixel.

[48] Yet another discretization scheme is ideal for  $F$  region drift patterns. In the auroral zone, there is often a uniform background convection superimposed with variations from ionospheric phenomena. The physical system is thus amenable to a multiscale basis expansion, such as Haar or another wavelet basis.

[49] The formulation of the estimation as an optimization problem is a common approach to regularization, and a multitude of strategies have been established to solve such problems. We have assumed Gaussian models and  $l^2$  norms, which leads to a solution that is a linear combination of the data. Modification of (3) (for instance, using non-Gaussian statistics or an  $l^1$  norm) results in other solutions, which are nonlinear and more difficult to obtain but potentially better suited to the problem.

[50] **Acknowledgments.** This material is based upon work supported by the National Science Foundation under grants DGE-0221680, ATM-0538868, and ATM-0547934. The authors are grateful to Donald Hampton for providing the optical data used in this work.

## References

- Aster, R. C., B. Borchers, and C. H. Thurber (2005), *Parameter Estimation and Inverse Problems*, Elsevier, New York.
- Bahcivan, H., D. L. Hysell, D. Lummerzheim, M. F. Larsen, and R. F. Pfaff (2006), Observations of colocated optical

- and radar aurora, *J. Geophys. Res.*, *111*, A12308, doi:10.1029/2006JA011923.
- Bristow, W. (2008), Statistics of velocity fluctuations observed by SuperDARN under steady interplanetary magnetic field conditions, *J. Geophys. Res.*, *113*, A11202, doi:10.1029/2008JA013203.
- de la Beaujardière, O., and R. Vondrak (1982), Chatanika radar observations of the electrostatic potential distribution of an auroral arc, *J. Geophys. Res.*, *87*(A2), 797–809, doi:10.1029/JA087iA02p00797.
- de la Beaujardière, O., R. Vondrak, and M. Baron (1977), Radar observations of electric fields and currents associated with auroral arcs, *J. Geophys. Res.*, *82*, 5051.
- Doupnik, J. R., A. Brekke, and P. M. Banks (1977), Incoherent scatter radar observations during three sudden commencements and a Pc 5 event on August 4, 1972, *J. Geophys. Res.*, *82*(4), 499–514.
- Fujii, R., S. Oyama, S. C. Buchert, S. Nozawa, and N. Matuura (2002), Field-aligned ion motions in the E and F regions, *J. Geophys. Res.*, *107*(A5), 1049, doi:10.1029/2001JA900148.
- Hagfors, T., and R. A. Behnke (1974), Measurement of three dimensional plasma velocities at the arecibo observatory, *Radio Sci.*, *9*(2), 89–93.
- Heinselman, C., and M. Nicolls (2008), A Bayesian approach to electric field and *E* region neutral wind estimation with the Poker Flat Advanced Modular Incoherent Scatter Radar, *Radio Sci.*, *43*, RS5013, doi:10.1029/2007RS003805.
- Hysell, D., G. Michhue, M. Nicolls, C. Heinselman, and M. Larsen (2009), Assessing auroral electric field variance with coherent and incoherent scatter radar, *J. Atmos. Sol. Terr. Phys.*, *71*(6–7), 697–707, doi:10.1016/j.jastp.2008.10.013.
- Lanchester, B. S., K. Kaila, and I. W. McCrea (1996), Relationship between large horizontal electric fields and auroral arc elements, *J. Geophys. Res.*, *101*(A3), 5075–5084, doi:10.1029/95JA02055.
- Menke, W. (1989), *Geophysical Data Analysis: Discrete Inverse Theory*, *Int. Geophys. Ser.*, Academic, New York.
- Nicolls, M., and C. Heinselman (2007a), Imaging of polar mesosphere summer echoes with the 450 MHz Poker Flat Advance Modular Incoherent Scatter Radar, *Geophys. Res. Lett.*, *34*, L20102, doi:10.1029/2007GL031476.
- Nicolls, M., and C. Heinselman (2007b), Three-dimensional measurement of traveling ionospheric disturbances with the Poker Flat Incoherent Scatter Radar, *Geophys. Res. Lett.*, *34*, L21104, doi:10.1029/2007GL031506.
- Semeter, J., T. Butler, C. Heinselman, M. Nicolls, J. Kelly, and D. Hampton (2008), Volumetric imaging of the auroral ionosphere: Initial results from PFISR, *J. Atmos. Sol. Terr. Phys.*, doi:10.1016/j.jastp.2008.08.014.
- Sulzer, M. P., N. Aponte, and S. A. González (2005), Application of linear regularization methods to Arecibo vector velocities, *J. Geophys. Res.*, *110*, A10305, doi:10.1029/2005JA011042.
- Tarantola, A. (2005), *Inverse Problem Theory and Methods for Model Parameter Estimation*, Soc. for Ind. and Appl. Math., Philadelphia, Pa.
- Weber, E. J., J. F. Vickrey, C. J. Heinselman, H. Gallagher, L. Weiss, R. A. Heelis, and M. C. Kelley (1991), Coordinated radar and optical measurements of stable auroral arcs at the polar cap boundary, *J. Geophys. Res.*, *96*, 17,847–17,863.

---

T. W. Butler and J. Semeter, Department of Electrical and Computer Engineering, Boston University, 8 St. Mary's St., Boston, MA 02215, USA. (butler@bu.edu; jls@bu.edu)

C. J. Heinselman and M. J. Nicolls, SRI International, 333 Ravenswood Ave., Menlo Park, CA 94025, USA. (craig.heinselman@sri.com; michael.nicolls@sri.com)